



Measurement of absolute response functions and detection efficiencies of an NE213 scintillator up to 600 MeV

Tsuyoshi Kajimoto^{a,*}, Nobuhiro Shigyo^a, Toshiya Sanami^b, Kenji Ishibashi^a, Robert C. Haight^c, Nikolaos Fotiades^c

^a Kyushu University, Motoooka, Nishi-ku, Fukuoka 819-0395, Japan

^b High Energy Accelerator Research Organization, Oho, Tsukuba, Ibaraki 305-0801, Japan

^c Los Alamos National Laboratory, Los Alamos, NM 87545, USA

ARTICLE INFO

Article history:

Received 5 September 2011

Received in revised form

31 October 2011

Accepted 20 November 2011

Available online 29 November 2011

Keywords:

Response function

Detection efficiency

Neutron

Time-of-flight

NE213 scintillator

SCINFUL-QMD

ABSTRACT

Absolute neutron response functions and detection efficiencies of an NE213 liquid scintillator that was 12.7 cm in diameter and 12.7 cm in thickness were measured for neutron energies between 15 and 600 MeV at the Weapons Neutron Research facility of the Los Alamos Neutron Science Center. The experiment was performed with continuous-energy neutrons on a spallation neutron source by 800-MeV proton incidence. The incident neutron flux was measured using a ²³⁸U fission ionization chamber. Measured response functions and detection efficiencies were compared with corresponding calculations using the SCINFUL-QMD code. The calculated and experimental values were in good agreement for data below 70 MeV. However, there were discrepancies in the energy region between 70 and 150 MeV. Thus, the code was partly modified and the revised code provided better agreement with the experimental data.

© 2011 Elsevier B.V. All rights reserved.

1. Introduction

An NE213 organic liquid scintillator is useful for measuring neutron energy spectra owing to suitable neutron–gamma pulse shape discrimination and time resolution. The neutron energy spectra are derived from the time-of-flight (TOF) or unfolding method. The TOF method requires precise neutron detection efficiencies, while the unfolding method requires accurate response functions.

The fundamental data required for obtaining a neutron energy spectrum are generally calculated using a Monte Carlo code such as OSS [1], STANTON [2], CECIL [3], or SCINFUL-QMD [4]. There are many experimental values at neutron energies below 20 MeV [5–8], and these codes reproduce the experimental response functions fairly well. Several experiments have been carried out at neutron energies above 20 MeV. However, some of these showed discrepancies between calculated and experimental data [9–11]. In addition, Satoh et al. [12] compared the measured response functions with the respective values calculated with the CECIL and SCINFUL-QMD codes, and found that the CECIL code generated rather large discrepancies for measurements above 300 MeV.

Neutron energy spectra from a thick copper target bombarded by 120 GeV protons were measured with NE213 scintillators [13]. In

this experiment, discrepancies between measured and calculated data were reported in the high energy region. To obtain more accurate neutron energy spectra, it is necessary to confirm the validity of the response functions and detection efficiencies calculated with these codes. Moreover, accurate data with high energy resolution are helpful for the further development of these codes.

In this study, we measured absolute response functions and detection efficiencies of an NE213 scintillator with 12.7 cm thickness and 12.7 cm diameter for neutron energies from 15 to 600 MeV. The kinetic energy of incident neutrons was determined by the TOF technique. The energy spectrum of incident neutrons was simultaneously measured using a ²³⁸U fission chamber to obtain absolute values of the response functions and detection efficiencies. Measured values were compared with the respective values calculated using the CECIL and SCINFUL-QMD codes. The accuracy of the calculations was improved by modifying the SCINFUL-QMD code. The detection efficiencies obtained using the modified code agreed to within 15% with the measurement data.

2. Experiment

2.1. Experimental setup

Fig. 1 shows the experimental setup. The experiment was carried out at the 4FP15L beam line of the Weapons Neutron

* Corresponding author. Tel./fax: +81 92 802 3484.

E-mail address: kajimoto@kune2a.nucl.kyushu-u.ac.jp (T. Kajimoto).

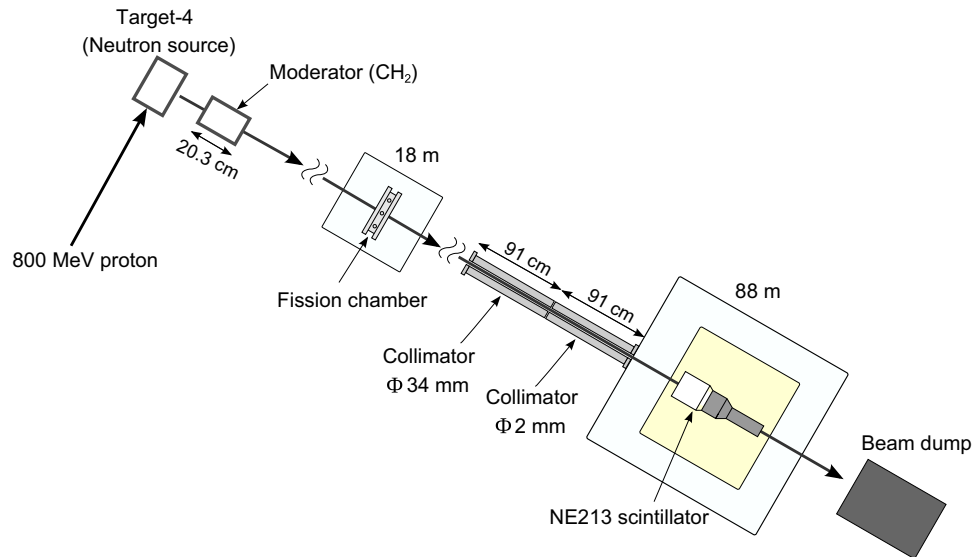


Fig. 1. Schematic view of experimental setup. Neutrons generated at a spallation target (Target-4) by 800-MeV proton incidence were used as incident particles. A polyethylene block was set close to Target-4 as a moderator to suppress low-energy neutrons. A fission chamber was set for the energy spectrum measurement of neutrons entering an NE213 scintillator. The NE213 scintillator having 12.7 cm diameter and 12.7 cm length was about 88 m downstream of Target-4. The shape of the neutron beam was limited by a collimator.

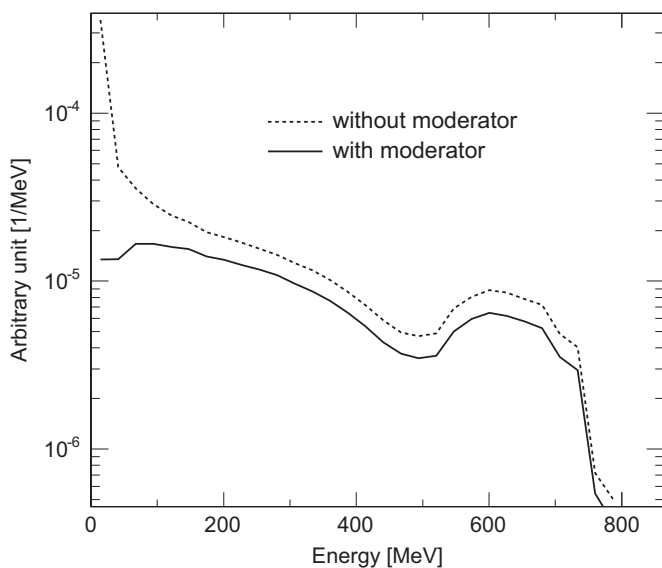


Fig. 2. Incident neutron flux calculated with the PHITS code for cases with and without the polyethylene moderator. Neutrons below 50 MeV are suppressed by the moderator.

Research (WNR) facility in the Los Alamos Neutron Science Center (LANSCE), which has an 800-MeV proton linear accelerator. The proton beam was bunched at less than 1 ns. The bunches were separated by 1.8 μ s (micropulse spacing) [14]. Neutrons were generated at a tungsten spallation target (Target-4) by proton incidence and were used as incident particles. A 20.3 cm thick polyethylene block was set close to Target-4 as a moderator to suppress low-energy neutrons. Fig. 2 shows the incident neutron flux calculated with the PHITS [15] code both with and without the moderator. The energy of the neutrons covers a wide energy range of up to 700 MeV.

The NE213 liquid organic scintillator used in the experiment was 12.7 cm in diameter and 12.7 cm thick. The scintillator was located 88 m downstream of Target-4. The diameter of the neutron beam was decreased to 2 mm by a brass and stainless

steel collimator. The outer diameter of the collimator was 18 cm, and the collimator completely sheltered the scintillator from the incident neutron beam. The collimator was set 2.7 m apart from the scintillator. The collimated beam was delivered to the center of the front plane of the scintillator. We estimated the effect of neutron scattering in the collimator using the PHITS code. The contribution of neutrons incident on the scintillator was less than 3%. The collimator had sufficient length.

A ²³⁸U fission ionization chamber [16] was used to measure the energy spectrum of the neutrons entering the scintillator. Since sufficient statistics of the fission chamber in front of the scintillator could not be obtained owing to the small beam size, the fission chamber was placed 18 m downstream of Target-4. The neutron beam cross-section was a square with 6.4-cm sides at the fission chamber position.

The measurements using the scintillator and the fission chamber were performed simultaneously. The number of incident neutrons was approximately 1000 per micropulse at the fission chamber position, whereas it was about one per micropulse at the scintillator position.

2.2. Electronic circuit

A simplified block diagram of the measurement circuit is shown in Fig. 3. The circuit consisted of standard NIM and CAMAC modules. When a micropulse signal (T0) arrives, a logic signal with length of 1.6 μ s is sent to the coincidence module (COIN). In case a logic signal from the scintillator arrives at the coincidence module while the T0 long logic signal is on, the coincidence module sends a trigger signal to a CAMAC controller for data acquisition. Once the data acquisition begins, the processes for further events are inhibited. The inhibition time was about 200 μ s, and the dead-time ratio of the data acquisition was 50%.

Recorded data included the total and slow components of the light output signal from the scintillator and the flight time from Target-4 to the scintillator. Charges of the analog pulse were recorded in charge-sensitive analog-to-digital converters (ADCs). Two different gate widths were set at the ADCs for particle identification. The flight time was measured with a time-to-digital converter (TDC). The TDC was started with a signal from

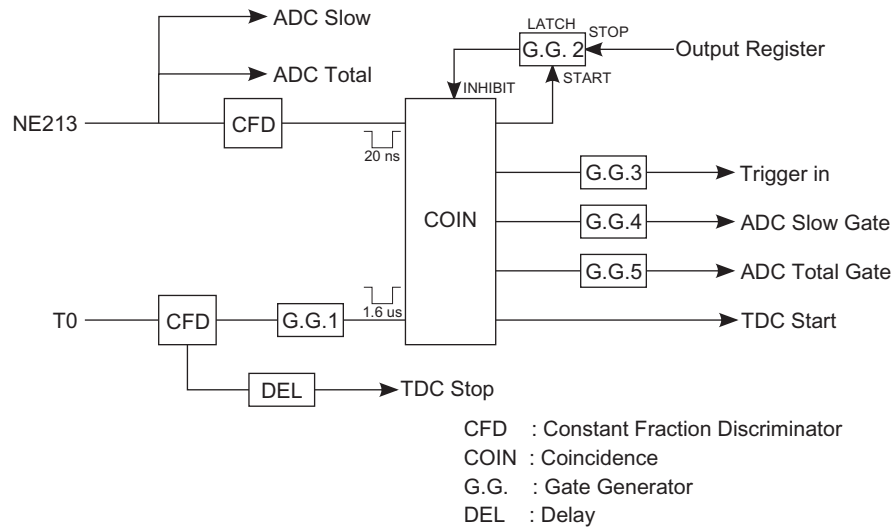


Fig. 3. Electronic circuit for recording scintillator data. The circuit consisted of standard NIM and CAMAC modules. Recorded data included total and slow charge amounts of an analog pulse from the scintillator and the time-of-flight. These data were recorded event by event.

the scintillator coincident with a T0 signal and stopped with the delayed T0 signal. Data of the ADCs and TDC were recorded event by event.

For the fission chamber, the electronic circuit in Ref. [16] was used. Recorded data included the pulse height of a signal and the flight time from Target-4 to the fission chamber. The data were acquired event by event.

3. Analysis

Response functions were derived from the following four analysis steps: (1) selection of neutron events by pulse shape discrimination, (2) determination of the neutron kinetic energy, (3) energy calibration of the light output, and (4) normalization by the number of incident neutrons. Detection efficiency was obtained by integrating a response function above a light output threshold. Data of the scintillator were analyzed in steps (1), (2), and (3). The number of incident neutrons in step (4) was obtained from the data of the fission chamber.

3.1. Analysis of the NE213 scintillator

Neutron events in step (1) were discriminated with the two-dimensional distribution of ADCs with total and slow gates, as shown in Fig. 4. Proton (p), deuteron (d), α particle (α), and electron (e) events were identified. The p, d, and α particles were produced by neutrons, and electrons were produced by γ -rays. Events relating to charged particles depositing their energy partially and escaping from the scintillator tend to overlap with those relating to γ -rays. Since it is impossible to discriminate the escaping charged-particle events from γ -ray events, we eliminated both types of events.

The kinetic energy of neutrons was determined by employing the TOF technique in step (2). The flight time of neutrons was derived from the difference between the arrival times of prompt γ -rays and neutrons. The neutron energy was converted from the flight time with relativistic kinematics. Fig. 5 shows the TDC distribution. In γ -ray and escaping events, we could observe two components. One is constant with the flight time and the other varies with the flight time. The constant component originates

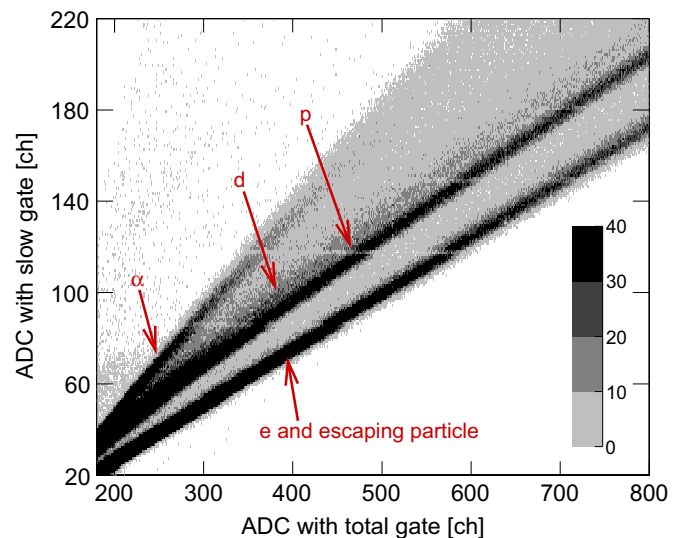


Fig. 4. Two-dimensional scatter plots of ADCs with the total and slow gate for selection of neutron events. The symbol e stands for the electron from a γ -ray, and p, d, and α are the proton, deuteron, and α particle produced by interaction with a neutron, respectively. Events of an electron and an escaping particle were eliminated.

from background γ -rays. The varying part arises from escaping particle events. The increase in incident energy leads to an increase in the probability of producing higher energetic charged particles. A higher energetic charged particle has a larger range and facilitates its emergence from the scintillator. Thus, the number of escaping events increases with the incident neutron energy.

In step (3), the total-gate ADC in units of the channel was converted into light output in units of electron-equivalent energy (MeVee). In the low light output region, Compton edges relating to γ -rays from ^{137}Cs and ^{60}Co sources were used to determine calibration points [17]. Furthermore, a calibration point was obtained from the Compton edge of the 4.4 MeV γ -ray resulting from the de-excitation of $^{12}\text{C}^*$ created by the interaction $^9\text{Be}(\alpha, n)^{12}\text{C}^*$ in the Pu–Be source. In the middle light output

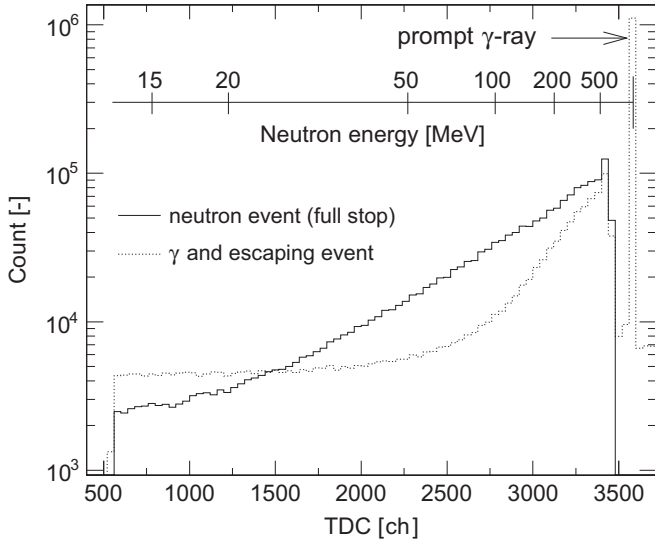


Fig. 5. TOF spectrum for the scintillator. The flight time of neutrons was determined using the prompt γ -ray peak and was converted into the neutron energy with relativistic kinematics. The dashed line represents the spectrum for electrons and escaping charged particles.

region, calibration points were obtained from the half height of the recoil-proton edge in the total gate ADC distribution at each neutron energy. The deposition energy corresponding to the recoil-proton edge was converted to the electron-equivalent light unit using the empirical formula [18]

$$T_e = 0.81T_p - 2.80[1.0 - \exp(-0.20T_p)], \quad (1)$$

where T_p and T_e are proton and electron energies, respectively. The recoil-proton edge was not observed above 120 MeV because high-energy protons penetrated the scintillator. Calibration points above 120 MeV were obtained by correlating maximum light outputs in the measurement data and calculations performed with the SCINFUL-QMD code.

3.2. Normalization

An energy spectrum of incident neutrons was deduced using the ^{238}U fission chamber [16]. The neutron spectrum ($d^2\phi/dE d\Omega$) in an energy bin with width dE , centered at an energy E , into a solid angle $d\Omega$ was determined as

$$\frac{d^2\phi(E)}{dE d\Omega} = \frac{C(E)}{\sigma_f(E)\rho_U\varepsilon\Delta E\Delta\Omega}, \quad (2)$$

where $C(E)$ is the number of fission events, $\sigma_f(E)$ is the $^{238}\text{U}(n,f)$ cross-section, ρ_U is the number density in the area of ^{238}U deposited on the foil of the chamber, and $\varepsilon = 0.98$ is the detection efficiency [16].

The fission events were discriminated from occurrences of the α decay of ^{238}U and particle knockout reactions, which provided much less energy to the chamber than the fission fragments. The neutron kinetic energy was determined by employing the TOF technique, which is based on the prompt γ -rays from Target-4.

We required neutron-induced ^{238}U fission cross-sections in a wide energy range between several MeV and several hundred MeV. Experimental values of Lisowski et al. [19] were adopted below 260 MeV, in addition to the data of the Japanese Evaluated Nuclear Data Library-High Energy File (JENDL-HE) [20] above 260 MeV. Fig. 6 presents ^{238}U fission cross-sections with several experimental values [21–23].

A correction for the attenuation of neutrons in air is required to obtain the neutron flux at the scintillator position because

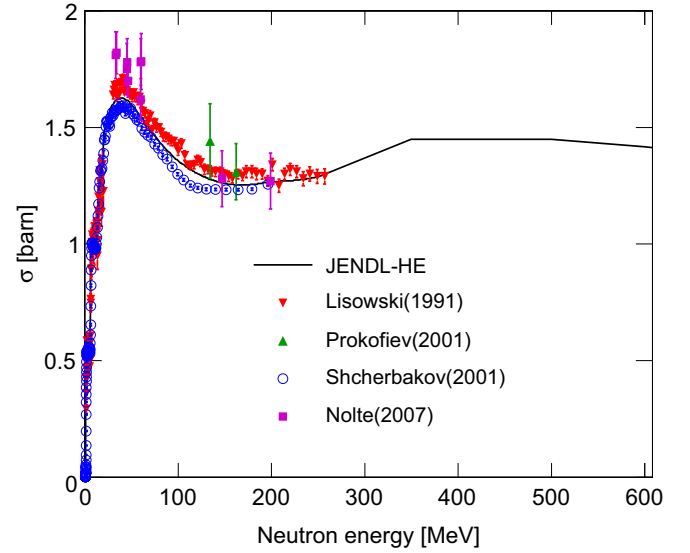


Fig. 6. Experimental and evaluated $^{238}\text{U}(n,f)$ cross-sections. Data of Lisowski et al. [19] were used to obtain the neutron energy spectrum, in addition to the data of the JENDL-HE file for neutron energies above 260 MeV.

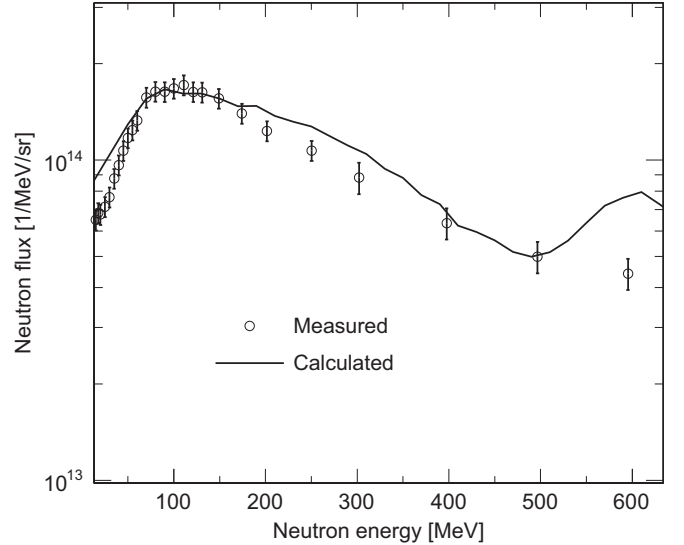


Fig. 7. Obtained neutron energy spectrum at a distance of 88 m from Target-4. For comparison, the relative energy spectrum calculated using the PHITS code is shown.

neutrons flow about 70 m through air from the fission chamber to the scintillator. The attenuation was estimated using the PHITS code coupled with the JENDL-HE file.

The obtained neutron energy spectrum is shown in Fig. 7 with relative values calculated with the PHITS code. The error bars include systematic and statistical uncertainties. The systematic uncertainty in the $^{238}\text{U}(n,f)$ cross-sections below 260 MeV was estimated to be 5% of the difference in experimental cross-sections reported by Lisowski and Shcherbakov. Since the experimental $^{238}\text{U}(n,f)$ cross-sections were not reported above 260 MeV, the uncertainty was estimated to be 10%. We added 5% error to the systematic uncertainty as a consequence of the discrimination of fission events, the number density of ^{238}U , and the air attenuation.

Since the calculated values were obtained with a simplified configuration, discrepancies are found between the measured and calculated data. In particular, the calculated values tend to differ

from the measured values above 500 MeV. This tendency is mainly related to the neutron spectrum from Target-4. There are some experimental values [24,25] in relation to thick target neutron yields for incident protons between several hundreds MeV and GeV. However, these data have not shown the same tendency as that of the calculated spectrum.

3.3. Energy resolution

The energy resolution σ of the TOF measurement is given by the expression

$$\frac{\sigma}{E} = \gamma(\gamma + 1) \sqrt{\left(\frac{\sigma_L}{L}\right)^2 + \left(\frac{\sigma_t}{t}\right)^2}, \quad (3)$$

where E is the neutron energy, γ the Lorentz factor, L the flight length, σ_L the uncertainty in the flight path, t the flight time, and σ_t the uncertainty in the flight time. The geometrical component σ_L was derived from the thicknesses of the target, moderator, and detector [26]. The time component σ_t was estimated by the proton bunch width (125 ps) of the accelerator and the full-width-at-half-maximum of the prompt γ -rays peak in the TOF spectrum. These values are given in Table 1. The energy resolutions of the TOF measurements using the fission chamber and the scintillator are shown in Fig. 8.

3.4. Contribution of neutrons from the preceding micropulse

Low-energy neutrons from the preceding micropulse overlapped with neutrons from the present micropulse owing to the long flight length. Since neutron energy was determined using the TOF technique, overlapping neutrons were regarded as misdirected energy events. However, it is possible to deduce the energy of overlapping neutrons by considering the micropulse interval of 1.8 μ s.

Fig. 9 shows the overlapping neutron energies at flight lengths for the scintillator and the fission chamber. The overlapping neutron energy was below 9 and 0.5 MeV for the scintillator

Table 1
Geometrical and time components of the energy resolution of TOF measurements.

Detector	Geometrical component (cm)	Time component (ns)
NE213	9.7	3.6
Fission chamber	6.2	3.8

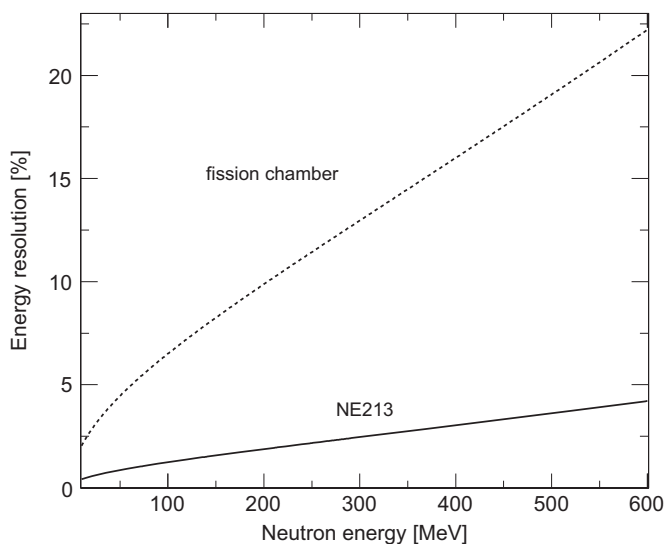


Fig. 8. Energy resolutions for TOF measurements in the scintillator and the fission chamber.

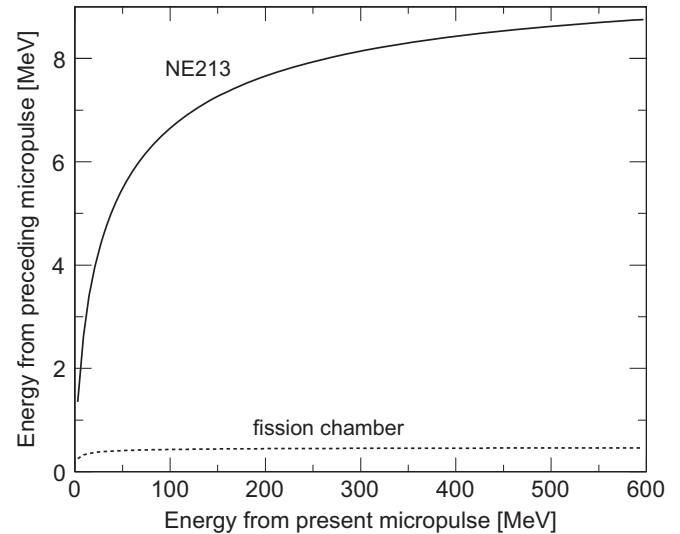


Fig. 9. Neutron energies from the preceding micropulse at flight lengths of the scintillator and the fission chamber.

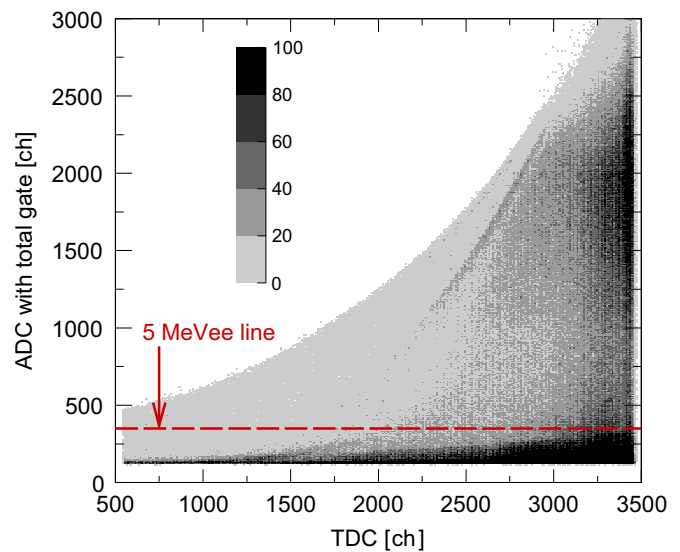


Fig. 10. Two-dimensional neutron plots for the TDC and ADC with the total gate. An increase in neutron events due to the preceding micropulse is observed in the low ADC channel region below 350 (5.0 MeVee). The low light output region includes neutron events not only from the present micropulse but also from the preceding micropulse.

and the fission chamber, respectively. Because the fission threshold of ^{238}U is approximately 1.5 MeV, the contribution was negligible in the derivation of the incident neutron number. For the scintillator, we observed an increase in the low light output region below 5 MeVee, as shown in Fig. 10, and it is impossible to correct for the contribution without assumptions. Therefore, we eliminated the light output region below 5 MeVee.

4. Results

4.1. Response function

Figs. 11–13 represent measured response functions for the incident neutrons of 15–600 MeV. The lower limit of the neutron energies is 15 MeV owing to the micropulse spacing. The upper limit is 600 MeV, which was determined by the time resolution of

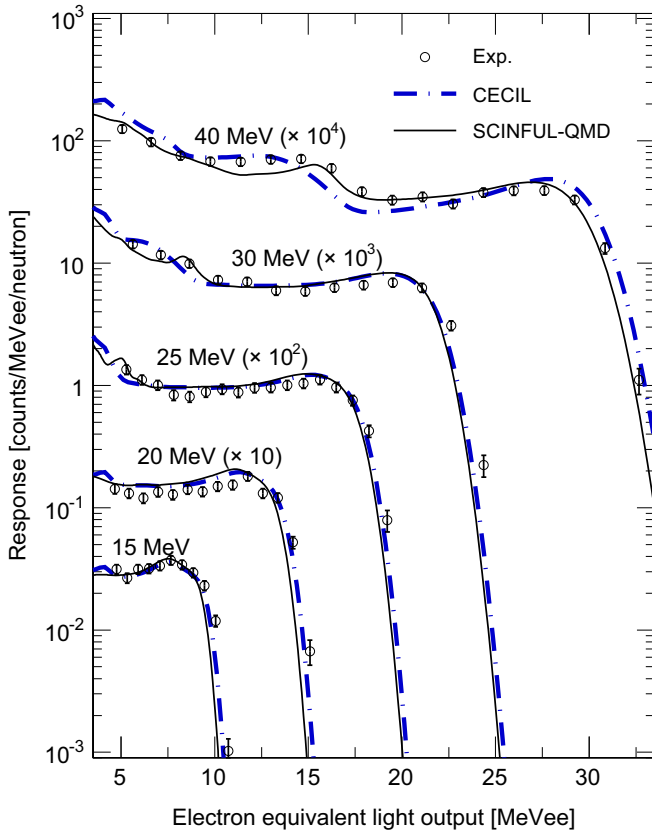


Fig. 11. Measured response functions for 15, 20, 25, 30, and 40 MeV neutron incidence. Experimental data are compared with the respective calculations with the CECIL and SCINFUL-QMD codes.

the TDC in the fission chamber. The error bars include the statistical errors relating to the scintillator and fission chamber and the systematic error relating to the fission chamber.

The measured data were compared with the respective values calculated with the CECIL and SCINFUL-QMD codes. Conditions of these calculations—the scintillator size, incident neutron direction, and position of neutrons incident on the scintillator—were the same as in the experiment. The contribution to light output from escaping charged particles was excluded from the experiment and calculations performed using the CECIL code. Since the SCINFUL-QMD code could not account for the elimination below 150 MeV, the calculations included escaping events. The calculated results from both codes were broadened to match the experimental data with a Gaussian function.

Below 150 MeV, the values calculated with the CECIL code are generally in good agreement with the measured results. Above 200 MeV, the calculations disagree with the measured data. The discrepancies are due to the simplified treatment of nuclear reactions in the code. Furthermore, only deposition energies of protons and α particles contribute to the light output.

The calculations with the SCINFUL-QMD code are in good agreement with measured data below 80 MeV. However, the calculated data are generally higher than the experimental data for the energy region between 100 and 150 MeV. The differences are due to the inclusion of escaping events. Disagreements are seen in the high light output region at neutron energies between 175 and 250 MeV. However, above 400 MeV, the measured response functions are in good agreement with the calculations. As mentioned above, calibration points in the high light output region were obtained as the maximum values in the ADC distribution corresponding to the maximum light output value

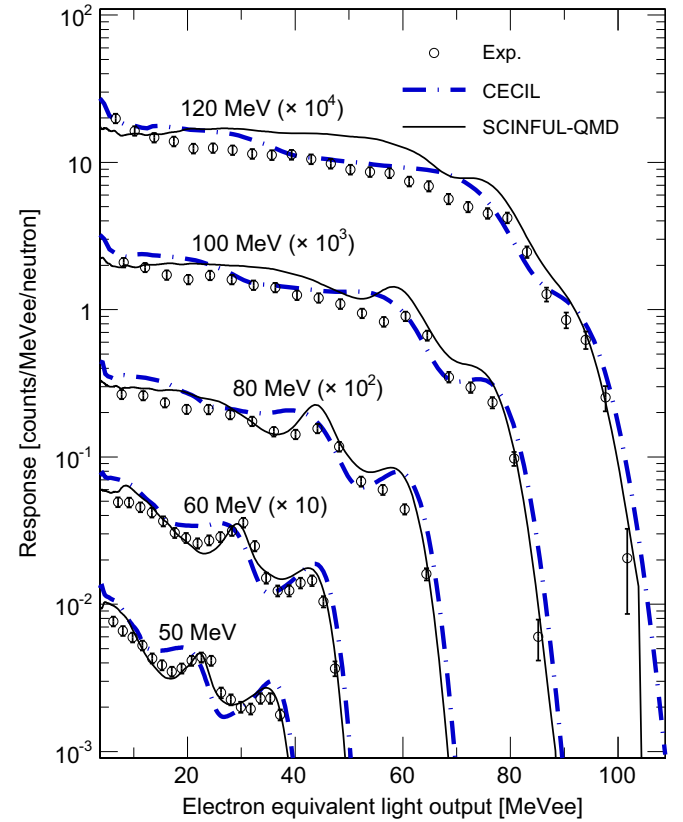


Fig. 12. Measured response functions for 50, 60, 80, 100, and 120 MeV neutron incidence. Experimental data are compared with the respective calculations with the CECIL and SCINFUL-QMD codes.

calculated with the SCINFUL-QMD code. Since the SCINFUL-QMD code does not necessarily give the correct maximum light output, it is difficult to assess the disagreements in detail.

4.2. Detection efficiency

Fig. 14 illustrates experimental detection efficiencies in comparison with the respective calculations with the CECIL and SCINFUL-QMD codes. Detection efficiency was obtained by integrating the response function above a specified light output threshold. The threshold was set at 5, 10, and 20 MeVee, and the contribution of the overlapping neutrons, as mentioned above, was not included. Furthermore, background neutrons were eliminated by setting a high threshold. The error was 7–11%.

Both calculations agree well with the experimental efficiencies below 40 MeV except for the 5 MeVee threshold data. Discrepancies below 30 MeV in the 5 MeVee threshold data are due to ambiguity in the calibration of the lower light output and the attenuation correction for the incident neutron flux. The calculations with the CECIL code do not reproduce the experimental tendency above 60 MeV. In the energy region between 70 and 150 MeV, the SCINFUL-QMD calculated data are higher than the experimental data for all thresholds. As described above, the deviations result from the inclusion of escaping events in the calculation. In addition, a sharp edge at 150 MeV is detected in the calculations. The SCINFUL-QMD code combines the SCINFUL code [27] below 150 MeV and a quantum molecular dynamics model incorporated with a statistical decay model [28] above 150 MeV. The energy of the edge corresponds to the switching energy. Above 200 MeV, the calculated values are lesser than the experimental data within 15% for all thresholds.

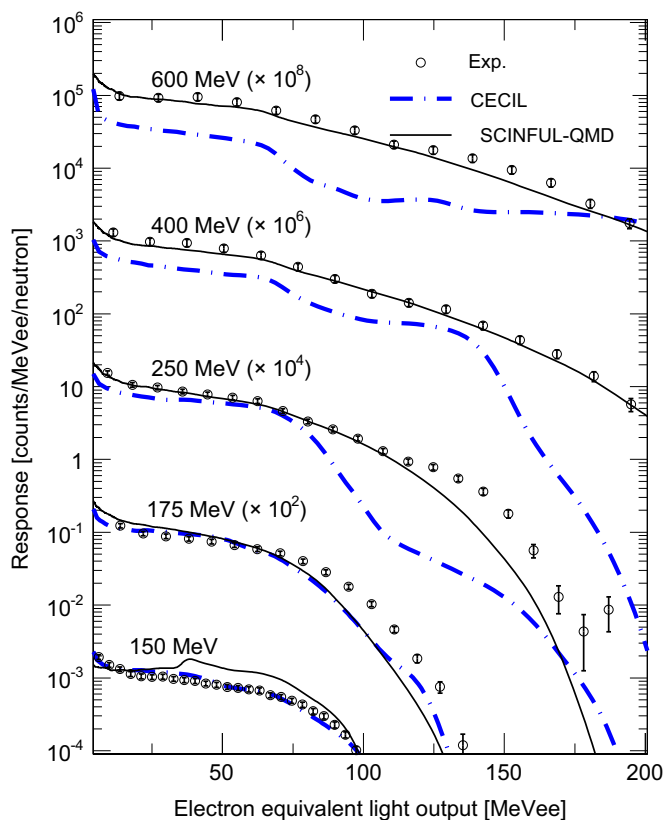


Fig. 13. Measured response functions for 150, 175, 250, 400, and 600 MeV neutron incidence. Experimental data are compared with the respective calculations with the CECIL and SCINFUL-QMD codes.

5. Modification of the SCINFUL-QMD code

This section describes the improvements in the SCINFUL-QMD code to reduce the differences between the experimental and calculated values. In particular, the improvements were attempted for the energy region between 60 and 150 MeV. The modifications relate to the handling of charged particles escaping from the scintillator below 150 MeV and reviews of $C(n,z)$ cross-sections.

5.1. Elimination of escaping events

Range data for some light ions are needed to determine whether a charged particle stops in the scintillator. Since proton range data were already used in the code, range data for deuteron and α particle were added to the code. The range data were based on results calculated with the SRIM code [29]. The code was modified as the light output of escaping events being zero when the energetic charged particle (proton, deuteron, or α particle) leaves the detector wall.

Fig. 15 shows the calculated efficiencies for an energetic charged particle escaping from the scintillator and experimental efficiencies for events eliminated in the neutron–gamma ray discrimination. The upper limit of the neutron energy was set to 150 MeV, which is the switching energy of the code. In the calculations, we set the same scintillator size, incident neutron direction, and position of the incident neutron relative to the scintillator as in the experiment. Only the energetic proton, deuteron, and α particle were traced in deciding events of particles from escaping the scintillator. In the experiment, events relating to γ -rays were almost eliminated by setting a higher light output threshold of 20 MeVee, while those of energetic charged particles escaping from the scintillator were kept. Errors related

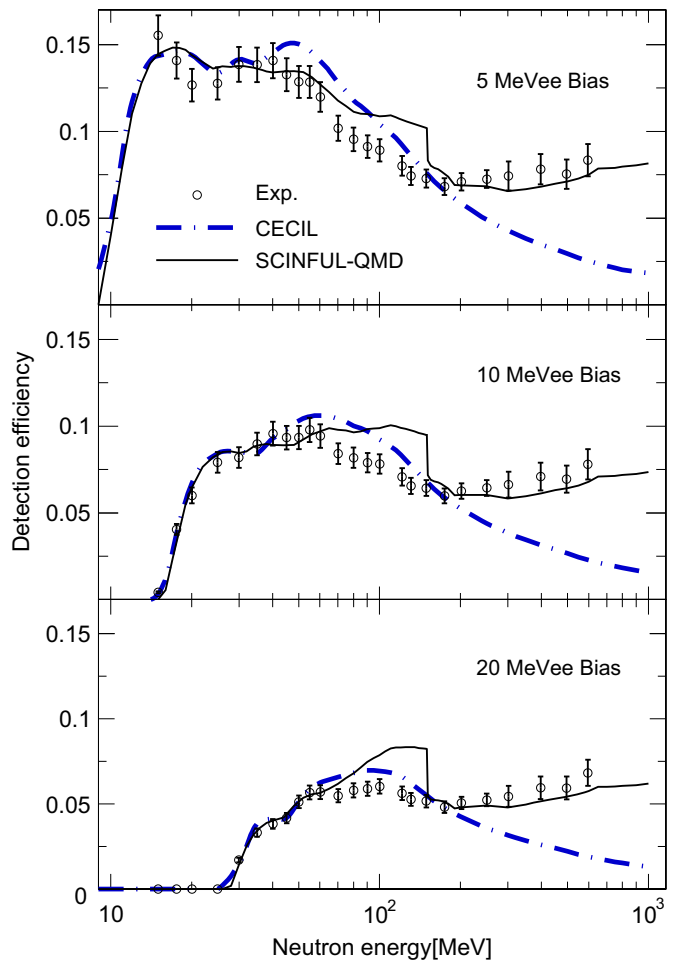


Fig. 14. Experimental neutron detection efficiencies of the scintillator. Circles are measured efficiencies for 5, 10, and 20 MeVee thresholds. Experimental data are compared with the respective calculations with the CECIL and SCINFUL-QMD codes.

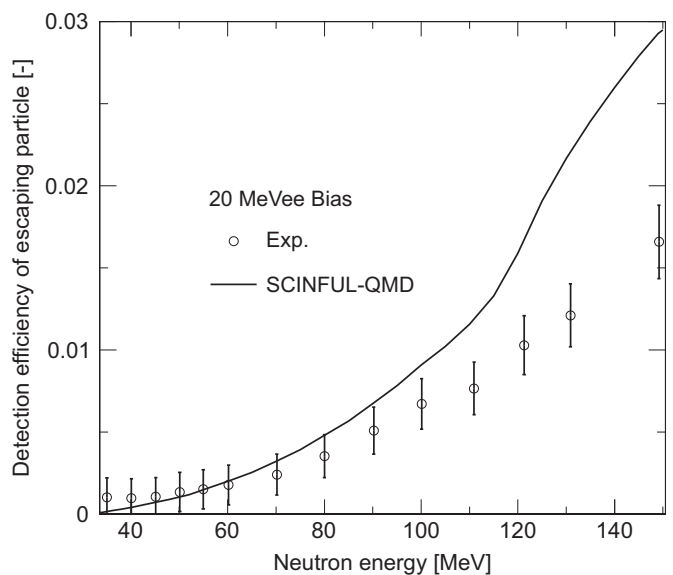


Fig. 15. Detection efficiencies of energetic charged particles escaping from the scintillator calculated with the SCINFUL-QMD code. Circles are experimental efficiencies for events eliminated in the neutron–gamma ray discrimination. The light output threshold is 20 MeVee. The proton, deuteron, and α particle were traced in determining escaping events in the calculations.

to γ -rays were added to each experimental error bar. The uncertainty was set at 0.001, i.e., the minimum efficiency in the low-energy region.

The experimental and calculated tendencies increased monotonically. The maximum energy of light ions produced in the scintillator increased as the incident energy increased, and the range also became larger with the light-ion energy. Therefore, the number of escaping particle events increased with increasing incident-neutron energy.

There is a difference between measured and calculated slopes, with the calculated results being higher than the experimental results above 60 MeV. In the calculations, the light output of escaping events was handled in a way similar to that of events relating to a charged particle stopping in the scintillator. The code could not consider the quenching effect originating from the difference between ionization densities of stopping and escaping events, and thus, overestimated the light output of escaping events.

5.2. Modification of $C(n,z)$ cross-sections

According to the calculations with the 5 MeVee threshold, the ratio of escaping-particle events to total detected events exceeded 10% at 90 MeV and became 35% at 150 MeV. The elimination of escaping events considerably affected the response functions and detection efficiencies. Furthermore, the effect depends on the position and direction of neutrons incident on the scintillator. If neutrons were to be induced to the entire front face of the scintillator, the effect would become larger. As we obtain accurate efficiencies and response functions under any condition, it is important to evaluate the exact number of escaping events. For such an evaluation, the accurate emission particle energy and angular distributions in $H(n,p)$ and $C(n,z)$ reactions as well as the range of light ions in the code are required. Meigo et al. [30] revised the total and differential n - p scattering cross-sections used in the code, and found that they were in good agreement with the experimental data. As mentioned above, range data had already been added to the code. We modified the energy and angular distributions of $C(n,z)$ cross-sections.

For $C(n,z)$ cross-sections, proton, deuteron, and α particle production cross-sections mainly contribute to response functions. We extracted these energy differential cross-sections from the code. Fig. 16 presents calculated energy differential $C(n, xp)$, $C(n, xd)$, and $C(n, x\alpha)$ cross-sections with experimental values [31]. The calculated energy differential $C(n, xp)$ cross-sections were much less than experimental data in the higher energy region. In the code, the energy distribution $\Phi(E)$ of a proton, deuteron, or α particle emitted by a neutron-carbon reaction is deduced as [27]

$$\Phi(E) = A \exp(E/T(E_n)) [1 - \exp(-E/B)], \quad (4)$$

where $T(E_n)$ is the nuclear temperature parameter at the incident neutron energy E_n (laboratory frame), A is the amplitude factor, B is the barrier penetration factor, and E is the energy of the emission particle in the center-of-mass frame. The energy of the emission particle is randomly determined to a value below the maximum energy. We phenomenologically modified $T(E_n)$ and $C(n,z)$ cross-sections in the code corresponding to the experimental values [31,32]. Modified calculations are shown in Fig. 16. The modifications result in agreement with the experimental values in the region of higher outgoing energy. Disagreements are seen in the lower outgoing energy region because the experimental values have pre-equilibrium and evaporation components, and it is difficult to reproduce the energy distribution with the formula.

For angular distributions of $C(n,z)$, we extracted double differential cross-sections in the code and compared them with the experimental values [31,32]. Experimental and calculated double

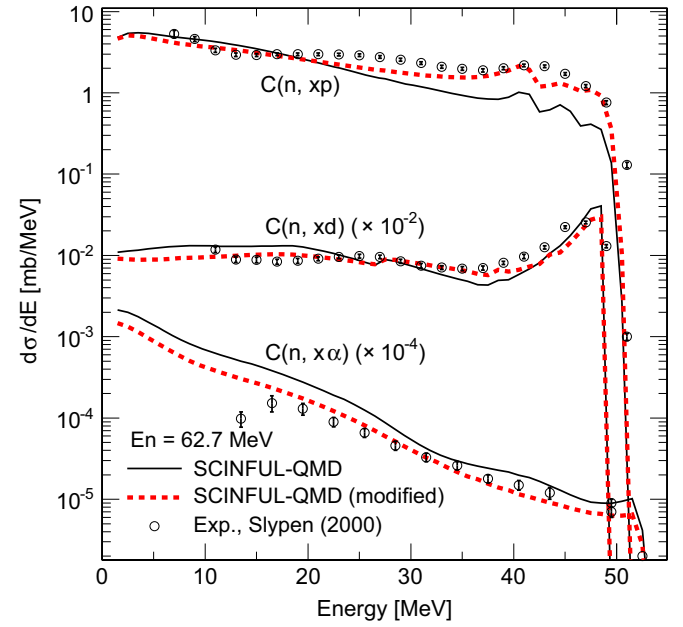


Fig. 16. Calculated and experimental [32] energy differential $C(n, xp)$, $C(n, xp)$, and $C(n, x\alpha)$ cross-sections. The incident neutron energy is 62.7 MeV. The calculated data were extracted from the code. Energy distributions in the code were modified to correspond to the experimental data phenomenologically.

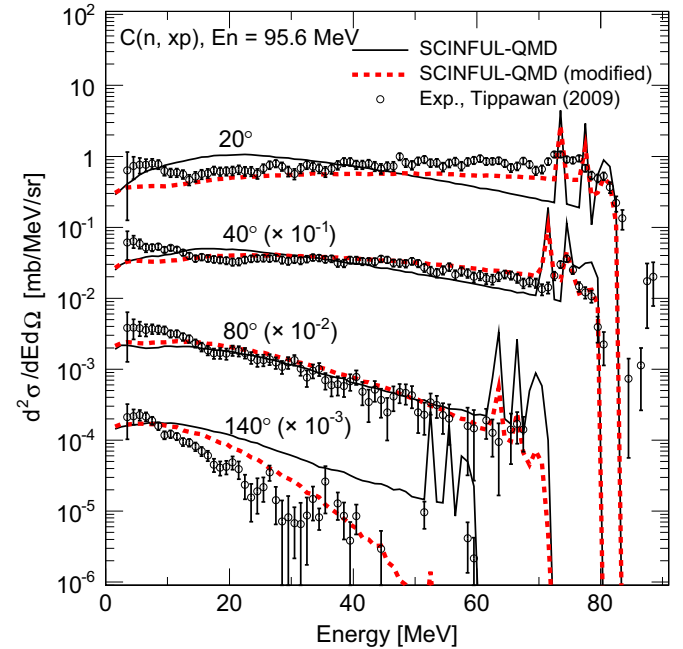


Fig. 17. Calculated and experimental [32] double differential $C(n, xp)$ cross-sections. The incident neutron energy is 95.6 MeV. The code was modified by applying Kalbach–Mann systematics to the angular distribution.

differential cross-sections of $C(n, xp)$ are shown in Fig. 17. The calculated values cannot reproduce experimental data for the forward angle in the higher energy region and for the backward angle. We applied Kalbach–Mann systematics [33] to the angular distributions of a proton, deuteron, or α particle emitted by the neutron-carbon reaction in the code. Modified proton emission calculations are also indicated in Fig. 17.

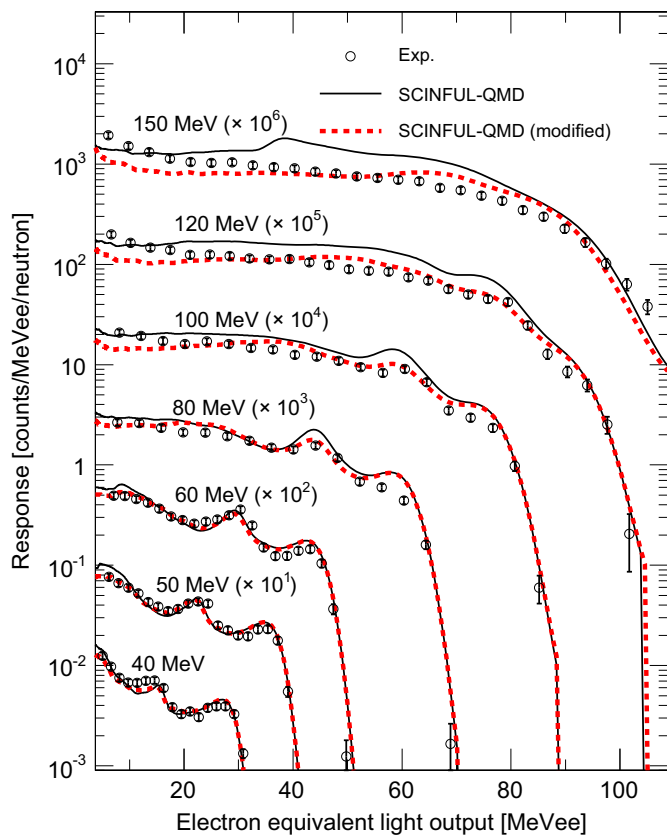


Fig. 18. Measured response functions for 40, 50, 60, 80, 100, 120, and 150 MeV neutron incidence. Experimental data are compared with the respective calculations from the original and modified codes.

5.3. Calculations with the modified SCINFUL-QMD code

Respective response functions calculated with the original and modified SCINFUL-QMD codes are displayed in Fig. 18 together with the experimental values. Modified calculations are in better agreement with the experimental data than the original calculations; however, the modified calculations still do not reproduce the tendency of the measured data for the energy region between 100 and 150 MeV. Since we forced the energy distributions of $C(n, z)$ to correspond with higher energy distributions, as mentioned above, there are differences in the light output region below 20 MeVee.

Respective detection efficiencies calculated with the original and modified code are illustrated in Fig. 19 together with the measured results. The modifications considerably improved efficiencies between 60 and 150 MeV. The modified calculations are in agreement with all measurement data to within 15%.

6. Summary

Absolute neutron response functions and detection efficiencies were measured for an NE213 scintillator that was 12.7 cm in diameter and 12.7 cm long at energies from 15 to 600 MeV with continuous-energy neutrons from a spallation target. The incident neutron flux was simultaneously measured by a ^{238}U fission chamber to obtain absolute values. The experimental detection efficiencies were deduced with high thresholds above 5 MeVee and had uncertainties of 7–11%.

The measured response functions and efficiencies were compared with the respective values calculated with the CECIL and SCINFUL-QMD codes. Response functions calculated with the

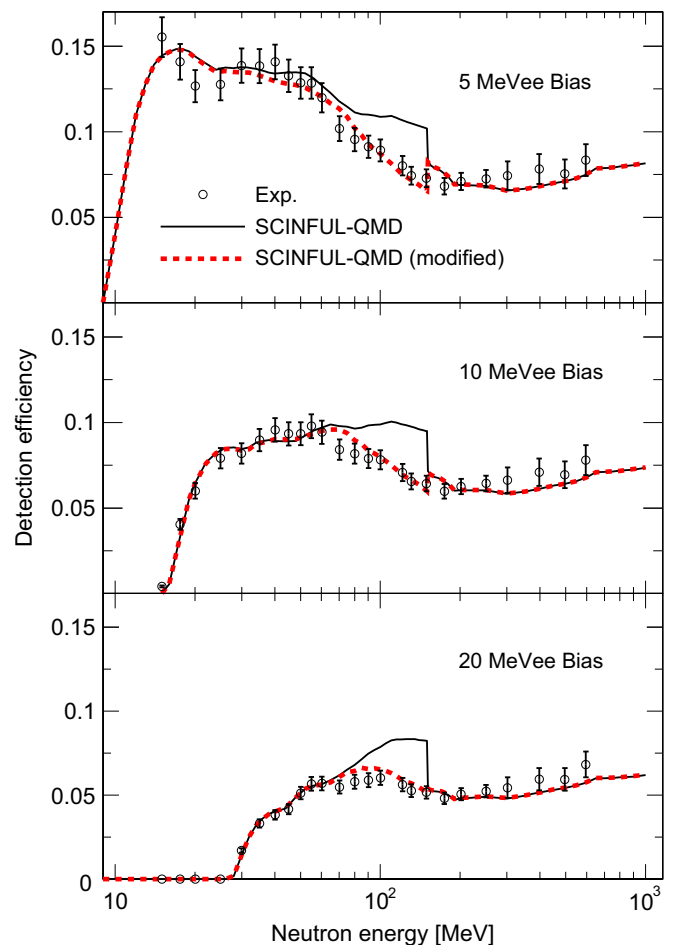


Fig. 19. Experimental neutron detection efficiencies of the scintillator. Circles represent measured efficiencies for 5, 10, and 20 MeVee thresholds. Experimental data are compared with the respective calculations performed using the original and modified codes. The modification provides good agreement with experimental values.

CECIL code were largely underestimated above 250 MeV. In the SCINFUL-QMD code, the calculated response functions were in good agreement with the experimental values except for the energy region from 100 to 150 MeV, where the code largely overestimated the response functions. In addition, the detection efficiencies were also overestimated for the energy region between 70 and 150 MeV.

To improve this situation, the SCINFUL-QMD code was modified such that the light output of escaping events is zero when the energetic charged particle (proton, deuteron, or α particle) leaves the detector wall. In the code, Kalbach–Mann systematics were applied to angular distributions of the neutron-induced light-ion production reaction for carbon. The modified calculations were in better agreement with the experimental data than the original calculations.

The detection efficiencies calculated with the original code were more than 25% larger than the experimental results at neutron energies between 100 and 150 MeV. The efficiencies obtained with the modified code were in agreement with the measured data to within 15%.

Acknowledgments

This study has benefited from the availability of the Los Alamos Neutron Science Center at the Los Alamos National

Laboratory. This facility is funded by the US Department of Energy under contract DE-AC52-06NA25396.

References

- [1] R.E. Textor, V.V. Verbinski, ORNL-4160, Oak Ridge National Laboratory, 1965.
- [2] N.R. Stanton, Ohio State University Report COO-1545-92, 1971.
- [3] R.A. Cecil, B.D. Anderson, R. Madey, Nuclear Instruments and Methods 161 (1979) 439.
- [4] D. Satoh, T. Sato, N. Shigyo, et al., JAEA-Data/Code 2006-023, 2006.
- [5] V.V. Verbinski, W.R. Burrus, T.A. Love, et al., Nuclear Instruments and Methods 65 (1968) 8.
- [6] M. Anghinolfi, G. Ricco, P. Corvisiero, et al., Nuclear Instruments and Methods 165 (1979) 217.
- [7] J. Cub, E. Finckh, K. Gebhardt, et al., Nuclear Instruments and Methods A 274 (1989) 217.
- [8] M.A. Al-Ohali, A. Aksoy, A. Cabana, et al., Nuclear Instruments and Methods A 396 (1997) 388.
- [9] N. Nakao, T. Kurosawa, T. Nakamura, et al., Nuclear Instruments and Methods A 463 (2001) 275.
- [10] J. Thun, J. Blomgren, K. Elmgren, et al., Nuclear Instruments and Methods A 478 (2002) 559.
- [11] S. Taniguchi, N. Nakao, H. Yamakawa, et al., Nuclear Instruments and Methods A 562 (2006) 954.
- [12] D. Satoh, T. Sato, A. Endo, et al., Journal of Nuclear Science and Technology 43 (2006) 714.
- [13] N. Shigyo, T. Sanami, T. Kajimoto, et al., in: Proceedings of the Tenth Meeting on Shielding Aspects of Accelerators, Targets and Irradiation Facilities (SATIF-10), Geneva, Switzerland, 2010, p. 65.
- [14] P.W. Lisowski, K.F. Schoenberg, Nuclear Instruments and Methods A 562 (2006) 910.
- [15] K. Niita, N. Matsuda, Y. Iwamoto, et al., JAEA-Data/Code 2010-022, 2010.
- [16] S.A. Wender, S. Balestrinit, A. Brown, et al., Nuclear Instruments and Methods A 336 (1993) 226.
- [17] G. Dietze, H. Klein, Nuclear Instruments and Methods 193 (1982) 549.
- [18] N. Nakao, T. Nakamura, M. Baba, et al., Nuclear Instruments and Methods A 362 (1995) 454.
- [19] P.W. Lisowski, A. Gavron, W.E. Parker, et al., in: Proceedings of the Specialists Meeting on Neutron Cross Section Standards for the Energy Region Above 20 MeV, Uppsala, Sweden, 1991, p. 177.
- [20] Y. Watanabe, K. Kosako, S. Kunieda, et al., Journal of the Korean Physical Society 59 (2011) 1040.
- [21] V.P. Eismont, A.V. Prokofyev, A.N. Smirnov, et al., Physical Review C 53 (1996) 6.
- [22] O. Shcherbakov, A. Donets, A. Evdokimov, et al., Journal of Nuclear Science and Technology Suppl. 2 (2002) 230.
- [23] R. Nolte, M.S. Allie, F.D. Brooks, et al., Nuclear Science and Engineering 156 (2007) 197.
- [24] S. Meigo, H. Takada, S. Chiba, et al., Nuclear Instruments and Methods A 431 (1999) 521.
- [25] K. van der Meer, M.B. Goldberg, E.H. Lehmann, et al., Nuclear Instruments and Methods B 217 (2004) 202.
- [26] International Organization for Standardization, Geneva, Switzerland, ISBN 92-67-10188-9, 1993, p. 17.
- [27] J.K. Dickens, ORNL Technical Report 6436, Oak Ridge National Laboratory, 1988.
- [28] K. Niita, S. Chiba, T. Maruyama, et al., Physical Review C 52 (1995) 2620.
- [29] J.F. Ziegler, J.P. Biersack, M.D. Ziegler, The Stopping and Range of Ions in Matter, SRIM.org, 2008.
- [30] S. Meigo, Nuclear Instruments and Methods A 401 (1997) 365.
- [31] I. Slypen, S. Benck, J.P. Meulders, et al., Atomic Data and Nuclear Data Tables 76 (2000) 26.
- [32] U. Tippawan, S. Pomp, J. Blomgren, et al., Physical Review C 79 (2009) 064611.
- [33] C. Kalbach, Physical Review C 37 (1988) 2350.